Biomedical Materials

OPEN ACCESS

RECEIVED
6 January 2026

REVISED
26 February 2026

ACCEPTED FOR PUBLICATION
25 March 2026

PUBLISHED
7 April 2026

PAPER

3D environment with BMP-2-releasing nanocarriers enhances osteogenic commitment of human tendon stem cells

Erwin Pavel Lamparelli[1,8], Adamo Lancellotti[1,8], Luigi Manzo[1], Giacomo Cortella[1], Antonio D'Ambrosio[2], Daniela De Cata[2], Vincenzo Piemonte[2], Joseph Lovecchio[3], Nicola Maffulli[6], Emanuele Giordano[4,5] and Giovanna Della Porta[1,7,*]

[1] Department of Medicine, Surgery and Dentistry, University of Salerno, via S. Allende, 84081 Baronissi, SA, Italy
[2] Unit of Chemical-Physics Fundamentals in Chemical Engineering, Department of Engineering, Università Campus Bio-Medico di Roma, Via Alvaro Del Portillo 21, 00128 Rome, Italy
[3] Research Unit of Intelligent Technology for Health and Wellbeing, Department of Engineering, Università Campus Bio-Medico di Roma, Via Alvaro del Portillo, 21, 00128 Rome, Italy
[4] Laboratory of Cellular and Molecular Engineering 'Silvio Cavalcanti', Department of Electrical, Electronic and Information Engineering 'Guglielmo Marconi' (DEI), University of Bologna, Cesena, FC, 47522, Italy
[5] Advanced Research Center on Electronic Systems (ARCES), University of Bologna, Bologna, BO 40126, Italy
[6] Department of Trauma and Orthopaedics, Faculty of Medicine and Psychology, Sant'Andrea Hospital, Sapienza University, 00189 Rome, Italy
[7] Research Centre for Biomaterials BIONAM, University of Salerno, via Giovanni Paolo II, 84084 Fisciano, SA, Italy
[8] The authors shared the first co-authorship.
[*] Author to whom any correspondence should be addressed.

E-mail: gdellaporta@unisa.it

Keywords: 3D bioprinting, tendon stem/progenitor cells (TSPCs), BMP-2 nanocarriers, osteogenic differentiation

Supplementary material for this article is available online

Abstract

This study presents a three-dimensional bioprinted scaffold engineered to promote the osteogenic differentiation of human tendon stem/progenitor cells (hTSPCs), isolated from tendon explants. The construct integrates human Bone Morphogenetic Protein-2 (hBMP-2)-loaded poly(lactic-co-glycolic acid) nanocarriers (PLGA-NCs; mean size 140 ± 40 nm) within a gelatin methacryloyl hydrogel. Bioprinting under optimized conditions preserved high cell viability (85%), ensuring a reliable platform for subsequent biological evaluation. Dynamic perfusion culture over 21 days supported continuous nutrient delivery and efficient removal of metabolic byproducts, as corroborated by compartmental modeling. This environment significantly enhanced hTSPCs proliferation and osteogenic commitment, evidenced by a 20-fold increase in osteopontin expression ($p < 0.05$), an 8-fold upregulation of osteocalcin ($p < 0.05$), and extensive calcium and protein deposition, confirmed by Alizarin Red S staining and Western blot analysis. In contrast, static monolayer cultures exposed to soluble hBMP-2 (20 ng ml^{-1}) exhibited reduced osteogenic activity, highlighting the superiority of the bioprinted dynamic system. The platform was specifically designed to provide a short, localized hBMP-2 pulse from PLGA-NCs, effectively priming early differentiation while minimizing overall growth factor exposure. These findings demonstrate the potential of combining biofabrication and NC-based delivery for spatiotemporally controlled growth factor presentation, paving the way for advanced *in vitro* models that more closely recapitulate complex tissue regeneration.

1. Introduction

Bone and its complex interfaces set up *in vitro* remains a major research frontier, fuelled by the pressing demand for innovative therapeutic strategies. To address these challenges, the integration of nanotechnology, stem cell biology, and advanced biofabrication techniques has emerged as a synergistic and highly promising pathway [1–3]. Particularly, gelatin methacryloyl (GelMA) bioink has attracted significant interest to fabricate *in-vitro* model, owing to its distinctive chemical structure and versatile functional properties [4–6].

GelMA is obtained by chemically modifying gelatin, a natural polymer derived from collagen, through methacrylation. This process introduces methacrylate groups into the protein backbone, enabling GelMA to undergo photo-crosslinking upon exposure to UV or visible light in the presence of a suitable photoinitiator [7, 8]. A key feature of GelMA is its excellent biocompatibility and biodegradability, which allow the hydrogel to be progressively remodeled and replaced by cell-deposited extracellular matrix (ECM). As such, GelMA is particularly well suited to provide temporary structural support while being gradually integrated into and substituted by newly formed ECM [9, 10].

BMP-2 is a growth factor widely recognized for its strong osteoinductive properties, facilitating the differentiation of mesenchymal stem cells (MSCs) into osteocyte precursors when adopted at concentration of 20 ng ml^{-1}; however, its use is limited due to short half-life [11]. To address this challenge, poly(lactic-co-glycolic acid) nanocarriers (PLGA-NC) formulations have been described to protect BMP-2 from premature degradation and also to enable its controlled and sustained release, improving therapeutic outcomes [11–14]. Among all the technologies for PLGA-NCs formulation [15, 16], microfluidics-assisted nanoprecipitation has emerged as a powerful method, providing superior control over nanoparticle size, uniformity, stability, and batch-to-batch reproducibility [17–19]. This method facilitated the production of both homogeneous and nanometric carriers, which can better assure controlled release properties [17, 20]. These growth factor reservoirs can be incorporated into a hydrogel matrix to create a spatiotemporally stratified microenvironment that better resembles the natural ECM [21, 22]. All these previous studies are related to immortalized cell lines or human bone marrow-derived MSCs in which 3D constructs were produced by simple casting approaches.

Human tendon stem/progenitor cells (hTSPCs) isolated from healthy human donors [23, 24] were used in the present study. They have been shown to exhibit multipotency, with the ability to differentiate into osteogenic, chondrogenic, and adipogenic lineages [24–26]. They also possess self-renewal capacity, a defining characteristic of stem cells, and express characteristic mesenchymal markers, including CD44, CD90, and CD105. These cells have further been characterized by their robust proliferative capacity while maintaining stemness, highlighting their suitability for regenerative medicine applications [24–26].

A wide range of carrier systems and bioprinting strategies have been developed to engineer cell culture microenvironments with controlled biochemical and biophysical cues [27–31]. In the context of BMP-2 delivery, PLGA and other functional polymeric carriers have been extensively investigated to create osteoinductive environments for tissue engineering applications [32, 33]. However, the majority of these studies have focused on conventional or non-tissue-specific cell types, such as immortalized cell lines or bone marrow-derived MSCs, to demonstrate osteogenic commitment [34, 35]. More recently, bioprinting approaches incorporating PLGA-based nanodevices for the controlled release of growth factors within 3D-printed constructs have been proposed using TSPCs; those cells have been reported to undergo tenogenic differentiation when cultured in the presence of growth differentiation factor 5 (GDF-5) [36–39].

Nevertheless, in those studies, TSPCs were not investigated for osteogenic differentiation, nor were they cultured within bioprinted 3D environments specifically designed to induce osteogenic commitment. To the best of our knowledge, the osteogenic differentiation of primary human TSPCs within a bioprinted, BMP-2-releasing 3D microenvironment has not been previously reported. Therefore, the present study addresses new insights into the use of tissue-specific primary stem cells for tendon-bone interface engineering.

When 3D bioengineered scaffold are cultured, is essential the exchange of functional biomolecules [40] and promote a convective mass transport; it is useful not only for catabolites but also to promote PLGA degradation and proper NCs release profiles. Indeed, mathematical modeling of the mass transport within dynamic culture often highlights its role in maintaining dynamic flow, enhancing nutrient delivery, and facilitating waste removal, and ultimately improving cellular function and tissue viability [22].

In this study, we described a three-dimensional (3D) GelMA culture platform specifically designed to provide a biomimetic microenvironment conducive to osteogenic commitment thanks to the sustained release of BMP-2 from loaded PLGA nanometric reservoirs embedded within. To our knowledge, this represents the first attempt to organize an ECM-mimicking environment to explore the osteogenic differentiation of hTSPCs within a controlled 3D setting. To further enhance physiological relevance, the 3D culture was performed under perfusion, providing a controlled environment for both BMP-2 release and cellular differentiation. The dynamic condition also promoted active mass transfer of metabolites as described by dynamic compartmental modeling of the scaffold environment. Cellular behavior was analyzed through quantitative real-time reverse transcription polymerase chain reaction (qRT-PCR), and western blotting to assess the expression of osteogenic markers and proteins, respectively, providing insights into the efficacy of the engineered system. Additionally, histology was conducted to validate the molecular and structural outcomes.

2. Materials and methods

2.1. hTSPCs harvesting

Semitendinosus tendon samples were obtained from three healthy donors (two males and one female; mean age 45 years) from surplus tissue generated during anterior cruciate ligament reconstruction procedures using autologous semitendinosus grafts. Tissue collection was approved by the local Ethics Review Board (prot. /SCCE n. 151, approved on 29 October 2020). Donors with comorbidities or with a history of tendon-related diseases were excluded from the study. hTSPCs were isolated from tendon biopsies using a previously optimized protocol and cryopreserved in liquid nitrogen until use [24–26]. Cells were cultured in minimum essential medium alpha (α-MEM; Corning Cellgro, Manassas, VA, USA) supplemented with 10% fetal bovine serum (FBS), 1% GlutaGro™, and 1% penicillin/streptomycin, and maintained at 37 °C in a humidified atmosphere containing 5% CO_2. Cells at passage 3 were used for all subsequent experiments.

2.2. NCs fabrication and characterization

PLGA (Resomer® RG 502 H, 7–17 kDa; Evonik, Essen, Germany) was dissolved in acetonitrile and used as the organic phase. Milli-Q® water supplemented with 1% (w/v) poly(vinyl alcohol) (molecular weight 30–70 kDa; Aldrich Chemical Co., Milan, Italy) was used as the aqueous phase. Human recombinant BMP-2 (hBMP-2; Millipore, Merck KGaA, Darmstadt, Germany) was reconstituted in a 0.1% (w/v) bovine serum albumin solution prior to encapsulation. PLGA-NCs were produced by nanoprecipitation using a microfluidic platform (iFlow™, Precigenome, USA) equipped with a passive staggered herringbone micromixer. The oil-to-water flow rate ratio was set to 1:3, with a total flow rate of 10 ml min^{-1}, as previously described [41]. Following production, NC suspensions were dialyzed (Spectrum Laboratories, Inc., USA) to remove residual solvent and free surfactant, and subsequently lyophilized (mod. ALPHA 1–4 LSC Plus, Deltek, Italy).

Particle size distribution and ζ-potential were determined by dynamic light scattering using a Zetasizer 1000HSa (Malvern Instruments, UK). NC morphology was assessed by field-emission scanning electron microscopy (FE-SEM, mod. LEO 1525, Carl Zeiss SMT AG, Oberkochen, Germany). Prior to imaging, samples were sputter-coated with a thin gold layer.

The loading was determined by dissolving 1 mg of PLGA-NCs in acetone, followed by peptide extraction via liquid–liquid extraction and its quantitative assays. The loading was calculated adopting the following equation (1):

$$\text{Loading ug/g} = \frac{W_{\text{BMP}-2}}{W_{\text{PLGA}}} \quad (1)$$

where $W_{\text{BMP-2}}$ is the total amount of encapsulated material expressed in ug, and W_{PLGA} is the total amount of polymer adopted during the NC preparation, expressed as g.

In-vitro BMP-2 release profile was evaluated over 21 d using 1.0 ± 0.3 mg of BMP-2–loaded PLGA NCs suspended in 500 µl of (α-MEM; Corning Cellgro, Manassas, VA, USA) containing 0.1% (v/v) Tween® 20. Samples were incubated at 37 °C under continuous agitation. At predetermined time points (every other day), samples were centrifuged at 14 000 rpm for 30 min, the supernatant was completely collected and replaced with fresh medium to maintain sink conditions. BMP-2 loading and concentration in the collected supernatants was quantified using a commercial ELISA kit (Human BMP-2 ELISA Kit, Cat. No. RAB0028; Sigma-Aldrich, USA). All release experiments were performed in triplicate ($n = 3$), and results are expressed as ng of BMP-2 released per g of PLGA NCs over time.

Table 1. Plotting parameters.

Print speed (mm s^{-1})	Bottom speed (mm s^{-1})	Travel speed (mm s^{-1})	Layer height (mm)	Fill density (%)
0.7	0.7	10	0.2	10

2.3. GelMA viscosity, bioprinting and 3D scaffold morphology

GelMA bioink (6% w/V GelMA Bioink with 0.25% LAP; CELLINK, Gothenburg, Sweden) was mixed with PLGA-NCs (1 mg ml^{-1}) and hTSPCs (1×10^6 cells m^{-1}) and bioprinted using a Rokit Dr INVIVO 4D2 bioprinter (Rokit Healthcare, Seoul, Republic of Korea) equipped with a 22-gauge nozzle. A summary of all bioprinting parameters is provided in table 1.

The rheological properties of the pure GelMA and GelMA supplemented with NCs (1 mg ml^{-1}) were evaluated at equal polymer concentration of 6% w/V, using a Kinexus rheometer (Malvern Panalytical Ltd, Malvern, UK) under steady-state flow conditions. Viscosity was recorded as a function of shear rate over a range of 0.01–100 s^{-1} at controlled temperature to characterize shear-thinning behaviour, which is critical for printability and structural fidelity during extrusion-based bioprinting. The printing bed temperature was maintained at 15 °C, while the extrusion chamber temperature was set to 26 °C. Both printing and travel speeds were set to 0.7 mm s^{-1}. A concentric infill pattern was selected, with a 90° rotation angle between successive layers. Cylindrical scaffolds (3.5 mm in diameter × 4 mm in height) were designed and sliced with a layer thickness of 0.2 mm using Creator K software (release 1.57.70). Scaffolds were printed onto Petri dishes and photocrosslinked by exposure to 405 nm UV light for 30 s.

For morphological analysis, scaffolds were fixed in 4% paraformaldehyde (PFA), dehydrated through a graded ethanol series, and freeze-dried. Samples were then fractured under liquid nitrogen for 2 min and imaged by FE-SEM as described before. Scaffold porosity was quantified by measuring Feret's diameter using ImageJ software and considering more than 50 SEM images (rel. 1.52p; NIH, Bethesda, MD, USA).

2.4. Dynamic culture asset

Following fabrication, scaffolds were transferred to a custom-made perfusion bioreactor and maintained under continuous perfusion for up to 21 d. The bioreactor consisted of a prototyped system integrating a peristaltic pump driven by a motor and controlled via an Arduino-based interface, enabling continuous medium perfusion at a flow rate of 1 ml min^{-1} within a multi-well plate format. The entire perfusion system was operated inside a standard cell culture incubator to maintain physiological temperature and gas conditions.

To further investigate and quantify the effects of dynamic perfusion on the scaffold microenvironment, a dynamic compartmental model was developed. Each well was represented by two interconnected compartments, corresponding to the culture medium (liquid phase, *l*) and the scaffold (solid phase, *s*). Within each compartment, the concentrations of nutrient (glucose) and waste (lactate) products were assumed to be spatially homogeneous in the corresponding phase, in accordance with previous experimental observations [22]. Under the assumptions of negligible cell proliferation and non-limiting oxygen conditions, a single well of the system can be described, in the absence of perfusion, by the following set of ordinary differential equations (equations (2)–(5)):

$$\frac{dC_N^l}{dt} = -K_C^N \cdot \frac{A_s}{V_l} \cdot \left(C_N^l - C_N^s\right) \quad (2)$$

$$\frac{dC_W^l}{dt} = +K_C^W \cdot \frac{A_s}{V_l} \cdot \left(C_W^s - C_W^l\right) \quad (3)$$

$$\frac{dC_N^s}{dt} = +K_C^N \cdot \frac{A_s}{V_s} \cdot \left(C_N^l - C_N^s\right) - g_N \cdot C_N^s \cdot \rho_{Cell} \quad (4)$$

$$\frac{dC_W^s}{dt} = -K_C^W \cdot \frac{A_s}{V_s} \cdot \left(C_W^s - C_W^l\right) + Y_{W/N} \cdot g_N \cdot C_W^s \cdot \rho_{Cell} \quad (5)$$

where C_N^i and C_W^i are the concentrations of nutrient and waste in the phase *i*. The glucose consumption in the solid phase, equation (4), was assumed as a first-order kinetic, with g_N representing the rate constant. The waste production is related to the glucose's consumption within the yield factor $Y_{W/N}$, equation (5). In the presence of perfusion, the mass balances in the liquid phase (equations (2) and (3)) include an additional convective term. This term accounts for the inflow of medium at a flow rate *Q*, carrying the concentration from the upstream well, and the outflow of an equal volume at the current well concentration (equations (6) and (7)):

$$\frac{dC_N^l}{dt} = -K_C^N \cdot \frac{A_s}{V_l} \cdot \left(C_N^l - C_N^s\right) + Q\left(C_N^{l,in} - C_N^l\right) \quad (6)$$

$$\frac{dC_W^l}{dt} = +K_C^W \cdot \frac{A_s}{V_l} \cdot \left(C_W^s - C_W^l\right) + Q\left(C_W^{l,in} - C_W^l\right). \quad (7)$$

A detailed description of the parameters and their corresponding values is provided in table 2. The mass transfer coefficients for nutrient K_C^N and waste K_C^W products were estimated using a phenomenological correlation valid for flow perpendicular to single cylinders [42] (equation (8)):

$$Sh = \left(0.35 + 0.34Re^{0.5} + 0.15Re^{0.58}\right) Sc^{0.3} \quad (8)$$

The dimensionless numbers required for the correlation, namely the Sherwood (Sh), Reynolds (Re), and Schmidt (Sc) numbers, were computed based on standard definitions using the characteristic dimensions and physical properties of the system, as also listed in table 2. The two sets of ordinary differential equations (equations (2)–(5) and (4)–(7)) were solved using gPROMS® (Process Systems Enterprise, Ltd.). Initial conditions were defined based on the concentrations of nutrient and waste in the unconditioned culture medium, for both the liquid and solid phases ($C_N^l(0) = C_N^s(0) = 5.55$ mol m^{-3}, $C_W^l(0) = C_w^s(0) = 2$ mol m^{-3}).

2.5. Live/dead assay and histology

Cell viability was assessed using a Live/Dead assay consisting of 2% calcein-AM and 1% propidium iodide (PI) (Sigma-Aldrich, Milan, Italy) immediately after bioprinting and after 14 and 21 d of culture. Samples were imaged using a fluorescence microscope (Eclipse series, Nikon Corporation, Tokyo, Japan) at 4× and 10× magnification. Quantitative analysis of fluorescent signal intensity was performed using ImageJ software (release 1.52p; NIH, Bethesda, MD, USA).

Calcium deposition was evaluated by Alizarin Red S staining (Santa Cruz Biotechnology, Inc., Dallas, TX, USA). At each time point, samples were washed three times with phosphate-buffered saline (PBS), fixed in 4% PFA for 2 h at room temperature, cryoprotected in 30% (w/v) sucrose at 4 °C overnight, embedded in optimal cutting temperature compound, and sectioned into 14 µm–thick slices using a CM1950 cryostat (Leica, Wetzlar, Germany) at −20 °C. Sections were mounted on polarized glass slides, incubated in Alizarin Red S solution for 45 min, and rinsed thoroughly with distilled water. Brightfield images were acquired using a microscope equipped with a Nikon D500 camera at 10× and 20× magnification.

Table 2. Model parameters. Summary of model parameters used in the compartmental dynamic simulations.

Parameter	Meaning	Value	Reference
V_s	Solid volume	$3.85 \cdot 10^{-8}\mathrm{m}^3$	[This work]
V_l	Liquid volume	$9.03 \cdot 10^{-6}\mathrm{m}^3$	[This work]
Q	Perfused flow rate	$1.67 \cdot 10^{-8}\mathrm{m}^3\,\mathrm{s}^{-1}$	[This work]
A_s	Lateral surface area of the cell scaffold	$4.40 \cdot 10^{-5}\mathrm{m}^2$	[This work]
g_N	Nutrient consumption velocity	$2.80 \cdot 10^{-9}\mathrm{m}^3/(\mathrm{s} \cdot \mathrm{cell})$	[43]
$Y_{W/N}$	Lactate/glucose yield factor	2	[43]
ρ_{Cell}	Cell density in the scaffold	$9.09 \cdot 10^{11}\,\mathrm{cell}\,\mathrm{m}^{-3}$	[This work]
D_N	Glucose diffusivity in the liquid medium	$3.9 \cdot 10^{-9}\mathrm{m}^2\,\mathrm{s}^{-1}$	[22]
D_W	Lactate diffusivity in the liquid medium	$1.6 \cdot 10^{-9}\mathrm{m}^2\,\mathrm{s}^{-1}$	[22]
h_s	Cell scaffold height	$4 \cdot 10^{-3}$ m	[This work]
ρ_l	Liquid density	$1000\,\mathrm{kg}\,\mathrm{m}^{-3}$	[22]
v	Average flow velocity	$8.3 \cdot 10^{-3}\mathrm{m}\,\mathrm{s}^{-1}$	[This work]
d_{in}	Inlet tube diameter	$1.6 \cdot 10^{-3}\mathrm{m}$	[This work]
μ_l	Liquid viscosity	$10^{-3}\mathrm{Pa} \cdot \mathrm{s}$	[22]

2.6. Gene expression by qRT-PCR

RNA was extracted from 3D scaffolds using Buffer RLT Lysis Buffer (RNeasy Micro Kit, Qiagen, Hilden, Germany). To ensure complete disruption of the mineralized and stiffened scaffold, samples were snap-frozen in liquid nitrogen and pulverized using a pre-chilled mortar. The resulting powder was resuspended in lysis buffer and homogenized by repeated pipetting. The lysate was then centrifuged, and the supernatant was processed following the manufacturer's instructions for RNA isolation with the RNeasy Micro Kit. For monolayer cultures, RNA extraction was performed directly after resuspending the cell pellet in Buffer RLT, following the standard kit protocol.

Isolated RNA was reverse transcribed into cDNA using the iScript™ cDNA synthesis kit (Bio-Rad, Milan, Italy). Quantitative gene expression analysis was performed on a LightCycler® 480 Instrument (Roche, Italy) using SsoAdvanced™ Universal SYBR® Green Supermix (Bio-Rad, Foster City, CA, USA) and validated primers for alkaline phosphatase (*ALP*), *COL1A1*, *OCN*, *OPN*, and *COL3A1* (Bio-Rad), in accordance with MIQE guidelines. All reactions were conducted in triplicate for each condition. Gene expression data were normalized to glyceraldehyde-3-phosphate dehydrogenase (GAPDH) as a reference gene, and fold changes were calculated using the $2^{-\Delta\Delta Ct}$ method relative to Day 0 (hTSPCs immediately after bioprinting). Experiments were performed in biological triplicates ($n = 3$).

2.7. Key osteogenic markers protein quantification via Western blot

Protein extraction was performed using the first elution obtained during RNA isolation with the RNeasy Micro Kit (Qiagen, Hilden, Germany). The eluted material was mixed with four volumes of ice-cold acetone and incubated at −20 °C to precipitate proteins. Precipitated proteins were collected by centrifugation, the supernatant was carefully removed, and the protein pellet was air-dried to remove residual solvent. Pellets were resuspended in RIPA buffer (EMD Millipore Corp., Burlington, MA, USA) supplemented with protease and phosphatase inhibitors, and protein concentration was determined using the bicinchoninic acid assay.

For Western blot analysis, 20 µg of protein per lane was mixed with Laemmli buffer, denatured at 95 °C for 5 min, and loaded onto 4%–20% Mini-PROTEAN TGX precast gels (Bio-Rad, Milano, Italy). Proteins were electrophoretically separated and transferred onto PVDF membranes using a semi-dry transfer system. Membranes were blocked with 5% non-fat dry milk in PBS-T (PBS 1× with 0.1% Tween-20) for 1 h and incubated overnight at 4 °C with primary antibodies against osteopontin, osteocalcin, and GAPDH (loading control). After washing with PBS-T, membranes were incubated with HRP-conjugated secondary antibodies for 1 h at room temperature. Protein bands were visualized using enhanced chemiluminescence and imaged with a ChemiDoc system (Bio-Rad). Densitometric analysis was performed using ImageJ software (release 1.52p; NIH, Bethesda, MD, USA), and target protein expression levels were normalized to GAPDH.

2.8. Statistical analysis

Statistical analyses were performed using GraphPad Prism (rel. 8.0; GraphPad, San Diego, CA, USA). All experiments were conducted in biological triplicates ($n = 3$), and data are presented as mean ± standard deviation (SD). Normality of the data was assessed using the Shapiro–Wilk test. For normally distributed datasets, statistical significance was determined using two-way analysis of variance. A p-value < 0.05 was considered statistically significant.

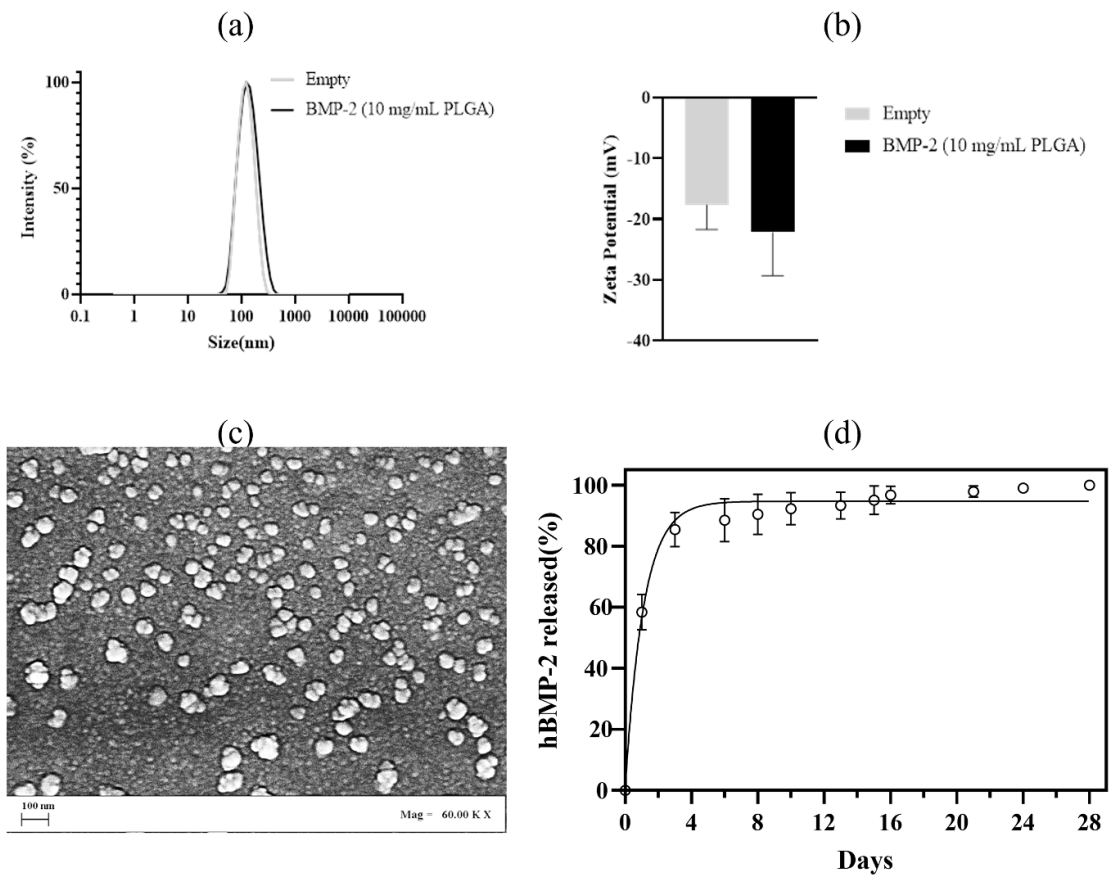

Figure 1. Physicochemical characterization of PLGA nanocarriers (PLGA-NCs). Dynamic light scattering analysis showing hydrodynamic mean diameter and polydispersity index of BMP-2–loaded and unloaded PLGA-NC formulations (a), together with corresponding ζ-potential measurements (b). Scanning electron microscopy (SEM) images confirm a spherical morphology with narrow size distribution and smooth surface topology for all formulations (c). Cumulative BMP-2 release profiles from PLGA-NCs in sink conditions and after encapsulation within the GelMA hydrogel matrix used in this study, demonstrating fast release behaviour within the 4–8 d of culture, following hydrogel incorporation in order to trigger the stem cells osteogenic commitment (d).

3. Results

3.1. PLGA-NCs fabrication by microfluidic

PLGA NCs were fabricated via nanoprecipitation using a microfluidic *Y*-shaped staggered herringbone micromixer (i.d. 600 µm; total channel length 20 mm). The organic (oily) phase was prepared at a concentration of 10 mg ml^{-1}, while BMP-2 was diluted to 1.33 µg ml^{-1} in the aqueous phase. A flow rate ratio of 1:3 was selected with a total flow rate of 10 ml min^{-1}. Batch volume recovery demonstrated a mean accuracy of 96%, indicating high reproducibility across production runs.

Under these conditions, BMP-2–loaded PLGA NCs exhibited a mean diameter of 144 ± 48 nm with a ζ-potential of −21 mV, whereas empty NCs showed a mean diameter of 133 ± 35 nm and a surface charge of −18 mV (figures 1(a) and (b)). SEM imaging confirmed that all NCs had a spherical morphology with smooth surfaces (figure 1(c)). The BMP-2 loading capacity was 0.16 µg BMP-2 per mg of PLGA, corresponding to an encapsulation efficiency of 60%. Incorporating 1 mg ml^{-1} of NCs into GelMA yielded a final BMP-2 concentration of approximately 159 ng ml^{-1}. The release profile exhibited a rapid initial phase, with ∼70% of the total BMP-2 released within 3 d and up to 90% by day 6, which seemed to be favorable for triggering osteogenic activity during the critical early stages of bone regeneration.

3.2. 3D scaffold architecture and cell viability

A schematic representation of the 3D-printed scaffold architecture is shown in figure 2(a) (top right corner). Each construct measured 3.5 mm in diameter and 4 mm in height, corresponding to a total volume of 38.5 mm^3, and was fabricated using 550 µl of GelMA containing 0.5 × 10^6 hTSPCs per scaffold. Bioprinting was performed at a speed of 0.7 mm s^{-1} with a 10% infill density and a layer height of 0.2 mm (see also table 1). Scaffolds were photocrosslinked using 405 nm UV light for 30 s. Under these conditions, BMP-2–loaded NCs were incorporated into the GelMA mixture at a concentration of ∼0.5 mg per scaffold, which did not compromise the printability

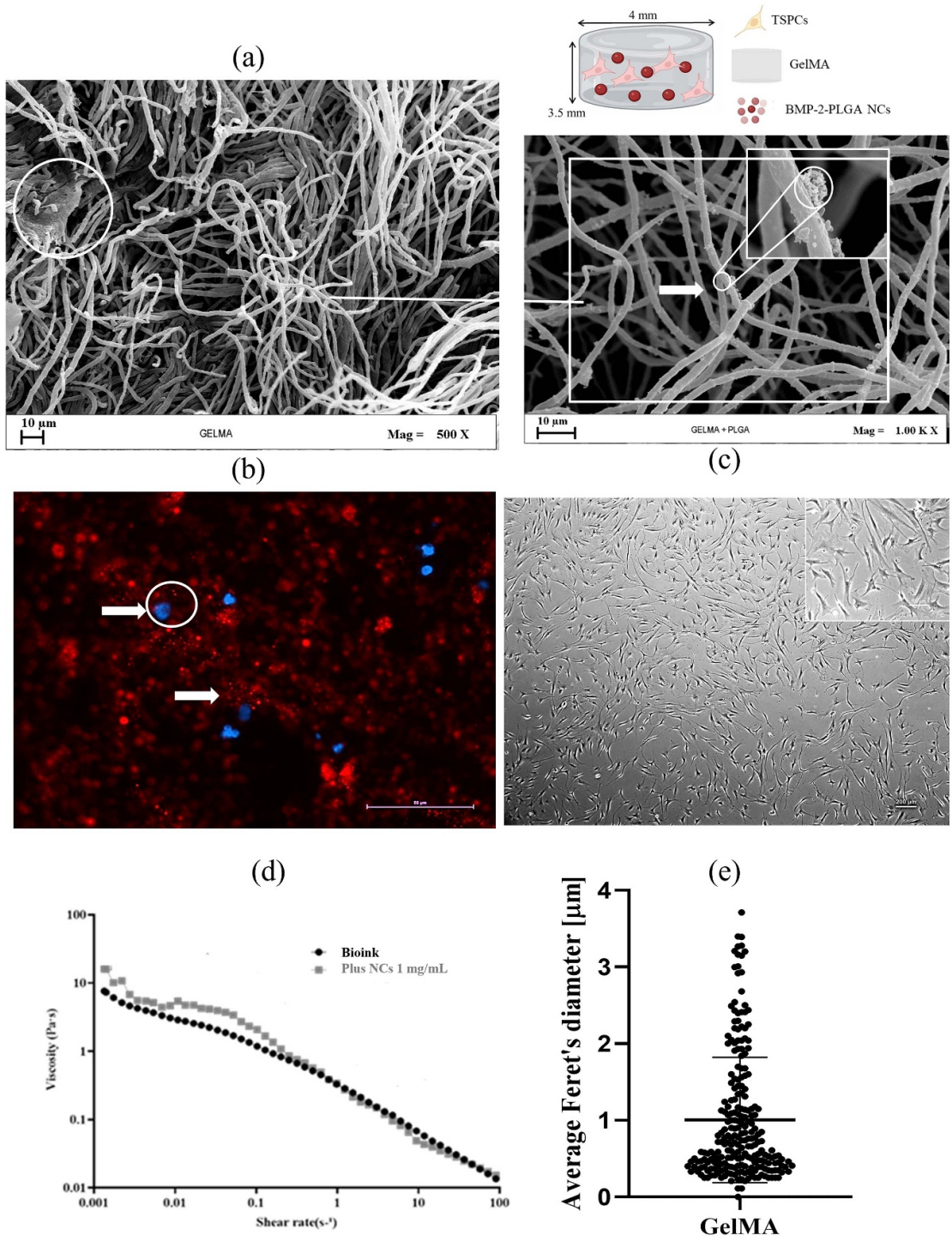

Figure 2. (a)–(f). Physicochemical and morphological characterization of GelMA and bioprinted 3D scaffolds. Field-emission scanning electron microscopy (FE-SEM) images showing the architecture of (dried) 3D scaffold with visible cells and nanocarriers (see white circles) and schematic representation of GelMA 3D environment (a). Confocal microscopy images of bioprinted scaffolds containing rhodamine-labeled PLGA-NCs (red), with cell nuclei stained with DAPI (blue), demonstrating homogeneous nanocarrier distribution within the 3D construct (b). Optical microscopy images of hTSPCs during expansion in standard 2D culture (c). Dynamic viscosity of GelMA hydrogel before crosslinking, measured for unloaded formulations and for formulations containing 1 mg ml^{-1} PLGA-NCs (d). Average Feret's diameter, calculated from SEM images using ImageJ software (e).

or structural integrity of the hydrogel. Indeed, SEM imaging confirmed a porous GelMA network with networked polymer fibers and the presence of PLGA-NCs throughout the 3D environment (figure 2(a)). Regarding the fiber-based geometry observed, it is important to note that this morphology is an artifact resulted by the drying of the hydrogel for SEM image acquisition. The bioprinted constructs are originally hydrogel-based systems with high water content (see schematic representation in supplementary

figure 1). To characterize the internal porosity, the scaffolds underwent a controlled dehydration/desiccation process. During this phase, the polymer chains within the hydrogel network are dried. This transition from a hydrated, bulk state to a dehydrated state leads to the formation of the observed fibrous microarchitecture. Therefore, the 'fibers' visible are the structural manifestation of the dried polymer matrix after the removal of the aqueous phase.

Confocal microscopy further demonstrated uniform NC distribution into the hydrogel, with rhodamine-labeled NCs shown in red and cell nuclei stained with DAPI in blue; in this sense, the apparent localization of NCs along gel fibers in SEM images is likely due to deposition during the freeze-drying process prior to imaging. hTSPCs displayed a typical fibroblast-like morphology when cultured in 2D monolayers (figure 2(c)), whereas in the 3D scaffold they adopted a more compact, rounded shape, as indicated by SEM (figure 2(b), dried cell highlighted with white circles). Incorporation of NCs did not significantly alter the hydrogel's dynamic viscosity (figure 2(d)), indicating that rheological properties and printability were preserved. After bioprinting and crosslinking, the average Feret's diameter of scaffold filaments ranged from 0.5 to 2 μm (figure 2(e)). This value seemed good for further medium perfusion along the culture.

Cell viability one day after bioprinting was approximately 85% (figure 3), indicating that the NCs concentration adopted (1 mg ml^{-1}) did not substantially increase the shear stress experienced by cells during extrusion. This observation is consistent with rheological analyses showing comparable dynamic viscosity values for GelMA formulations with and without NC incorporation (figure 2(d)), as previous stated.

Constructs were subsequently cultured under dynamic perfusion at a flow rate of 1 ml min^{-1}, providing a stable and well-nourished 3D microenvironment. Although a slight decrease in cell viability was observed at day 14, viability recovered to approximately 95% by day 21. At this later time point, cells exhibited more elongated morphologies, suggesting adaptive changes in cell behavior consistent with lineage-specific responses (figures 3, 21 d).

3.3. Mathematical modeling of nutrient and catabolite distribution: static vs dynamic environment

Dynamic compartmental modeling results, illustrated in figures 4(b) and (c) color maps from day 0 to day 3, highlight the significant impact of perfusion on spatial homogeneity. In the case of glucose, the average concentration difference between the liquid and solid compartments remained relatively small under both conditions (0.45 mol m^{-3} in the static case vs. 0.05 mol m^{-3} under perfusion), indicating a reasonably effective diffusion process even without flow. However, the accumulation of lactate showed a much more pronounced contrast: while static conditions led to an average concentration difference of 1.7 mol m^{-3}, dynamic perfusion reduced this value to 0.2 mol m^{-3}. This observation is particularly important, as it highlights that the dynamic culture conditions not only supported cell viability but also facilitated the proper release of the growth factor from the PLGA reservoir. This ensured the maintenance of appropriate sink conditions within the hydrogel environment, promoting effective and sustained bioavailability of hBMP-2 throughout the construct.

3.4. Calcium phosphate deposition: 2D vs 3D culture

Alizarin Red S staining was employed to detect calcium phosphate deposits as an indicator of matrix mineralization and osteogenic differentiation. During osteogenic commitment, hTSPCs acquire an osteoblast-like phenotype and deposit mineralized matrix, which binds Alizarin Red S and allows visualization of bone-like tissue formation. In the present study, staining intensity was used qualitatively to reflect the extent of mineral deposition. Conventional 2D monolayer cultures supplemented with soluble hBMP-2 (20 ng ml^{-1}) under static conditions were included exclusively as a reference condition for comparison (figure 5, left). In this setting, mineral deposition was detectable only at day 21, and the overall staining intensity appeared limited, likely due to the repeated medium changes inherent to 2D static culture, which may partially wash out loosely bound calcium deposits. In contrast, hTSPCs cultured within 3D GelMA scaffolds under dynamic perfusion exhibited markedly stronger and progressively increasing Alizarin Red S staining over time (figure 5, right). Notably, clear mineral deposition was already evident at days 7 and 14, indicating that the 3D dynamic microenvironment not only supported cell viability but also promoted earlier and more robust osteogenic commitment. These findings also highlight the advantages of the perfused 3D environment in maintaining mineralized matrix, varying its stiffness along the culture and enhancing osteogenic differentiation of TPSCs retained within compared with conventional 2D static culture.

3.5. Osteogenic commitment by gene and protein evaluation: 2D vs 3D culture

Quantitative real-time PCR (qRT-PCR) analysis of osteogenic gene expression in hTSPCs cultured under different conditions over 21 d is presented in figure 6. Cells were either maintained in conventional 2D monolayer (static) culture with soluble BMP-2 supplementation (20 ng ml^{-1}) or cultured within 3D bioprinted GelMA scaffolds under dynamic perfusion, where BMP-2 was delivered in a controlled manner via PLGA NCs. A clear divergence in osteogenic

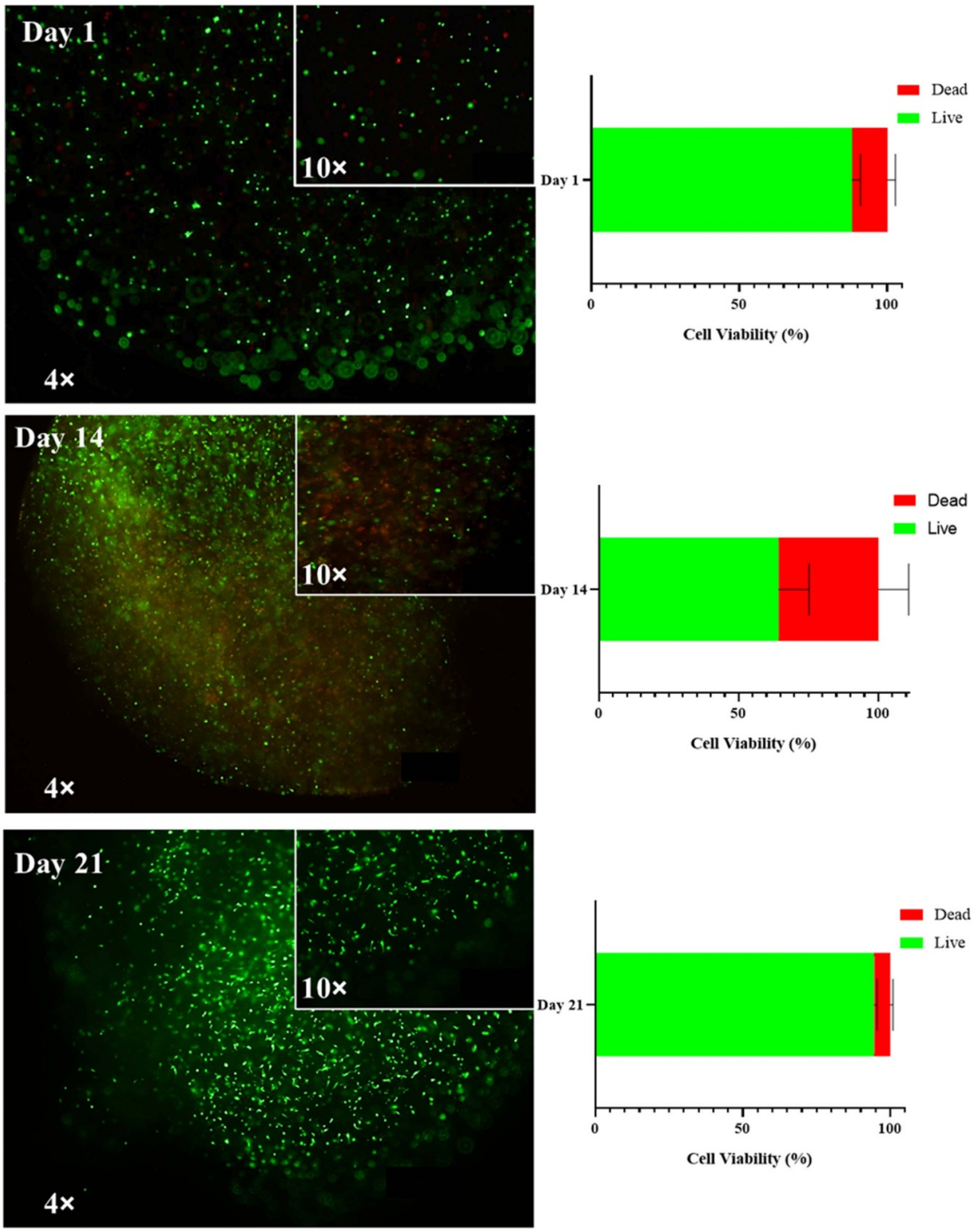

Figure 3. Live/dead assay on hTSPCs bioprinted scaffolds. hTSPCs were used to bioengineer 3D GelMA scaffolds and cultured under perfusion for 21 d. Live/dead assay was performed at every culture time-point (0, 7, 14, and 21 d) and images were acquired at 10× magnification; live cells are stained in green while dead cells are stained in red. $n = 3$ (biological replicates). Magnification: 4 and 10 × .

commitment was observed between the two culture systems. Under 3D dynamic conditions, hTSPCs exhibited a markedly enhanced and sustained osteogenic gene expression profile. ALP, an early marker of osteogenesis, increased approximately 5-fold in the 3D perfused scaffolds, whereas only a modest ∼1-fold increase was detected in 2D monolayer culture, indicating a limited early osteogenic response in the latter. Similarly, osteopontin (OPN) expression was significantly higher in the 3D environment. While OPN was upregulated in both conditions at day 21, the magnitude of expression was substantially greater under dynamic 3D culture (≈20.9-fold) compared with 2D static culture (≈11.7-fold; $p < 0.05$). Late-stage osteogenic markers followed the same trend. Osteocalcin (OCN) and type I collagen

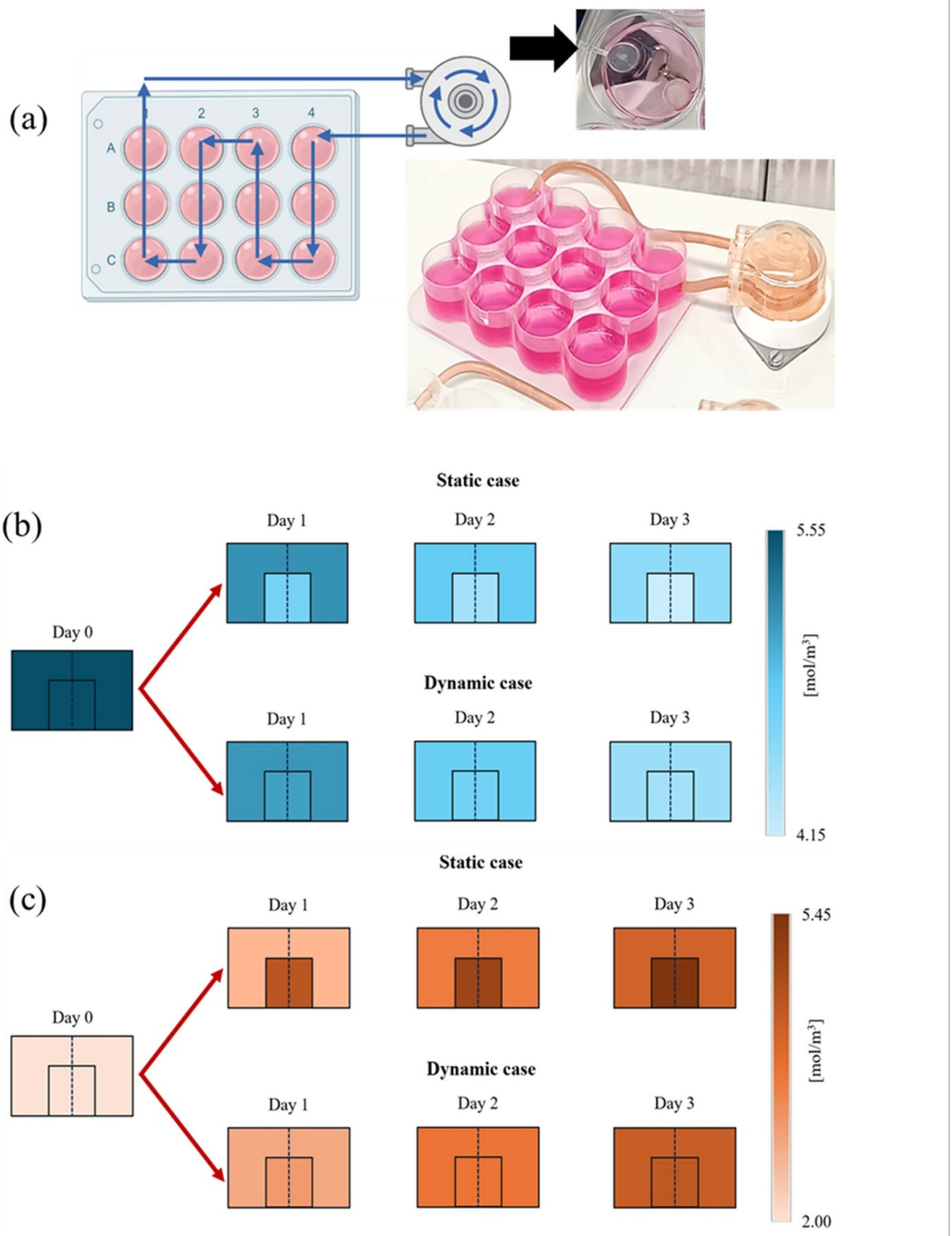

Figure 4. (a)–(c). Perfusion bioreactor illustration and dynamic compartmental modeling of mass transport under perfusion culture. Schematic representation of the perfusion flow generated by a peristaltic pump driven by an Arduino-controlled motor and image of the adopted bioreactor (a). Dynamic compartmental modeling employed to evaluate mass transfer phenomena at the scaffold–medium interface under continuous perfusion (1 ml min^{-1}). The model describes the spatial distribution of nutrients (b) and metabolic waste products (c) within the 3D bioprinted construct and the surrounding culture medium. Convective transport induced by perfusion flow and diffusive transport within the GelMA matrix were both considered to predict concentration gradients across the scaffold thickness. The simulations demonstrate efficient nutrient supply and waste removal throughout the construct.

(COL1A1) showed more robust and temporally sustained expression in the 3D perfused scaffolds, consistent with progressive matrix maturation. 3D culture of TPSCs without supplemented growth factor do no showed any proper commitment nor osteogenic gene expression (data not shown).

These transcriptional findings were corroborated at the protein level by Western blot analysis (figures 7(a) and (b)). In 3D dynamic cultures, both OPN and OCN were clearly detectable at all time points, with increasing band intensity over time. In contrast, 2D static cultures showed a transient and less stable osteogenic response: OCN expression peaked at day 7 and became undetectable at later time points, whereas OPN increased modestly and only became clearly detectable by day 21. Densitometric analysis confirmed a substantially stronger and more sustained upregulation of OPN in

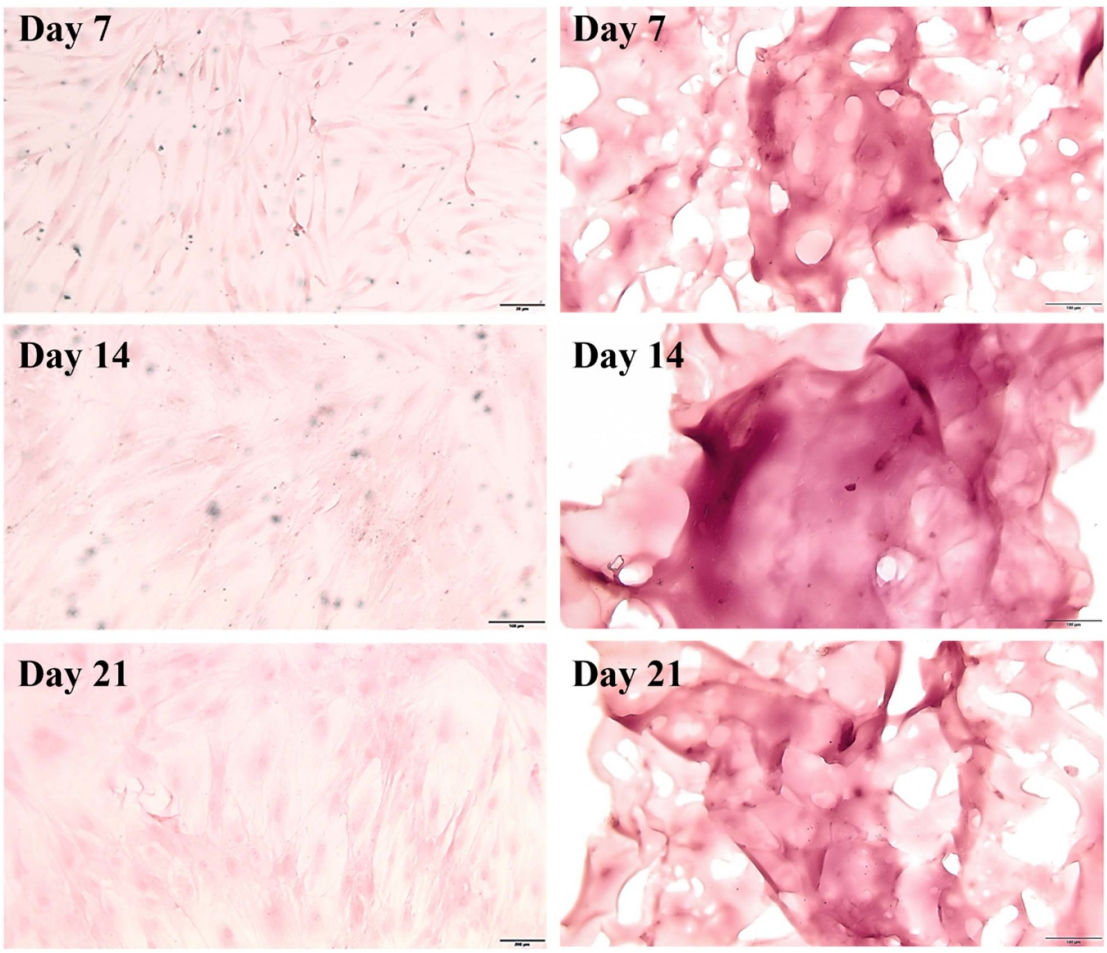

Figure 5. Alizarin Red S staining of hTSPCs cultured in 3D bioprinted GelMA scaffolds under dynamic perfusion for up to 21 d. Calcium phosphate deposition within the extracellular matrix was evaluated at different time points using Alizarin Red S staining. Representative images of hTSPCs cultured under conventional 2D static conditions with soluble BMP-2 supplementation are included for comparison. Magnification: 10 × .

the 3D environment, reaching approximately 28-fold by day 21 compared with a ∼4-fold increase in 2D cultures ($p < 0.05$).

Overall, these data demonstrate that the 3D bioprinted GelMA scaffolds under dynamic- perfusion, combined with nanoparticle-mediated BMP-2 delivery, provide an effective microenvironment for driving osteogenic differentiation of hTSPCs.

4. Discussion

BMP-2 is a key member of the bone morphogenetic protein family, a subgroup of cytokines and growth factors within the TGF-β (transforming growth factor-beta) superfamily. It plays a pivotal role in bone development, primarily by regulating cell differentiation with osteogenic commitment. The optimization of BMP-2–loaded PLGA NCs was guided by the mechanochemical model proposed by Ribeiro *et al* [11], which emphasizes the importance of growth factor dosage and presentation kinetics in regulating stem cell commitment toward an osteogenic phenotype. According to this framework, a controlled and transient ('pulse') delivery of Bone Morphogenetic Protein-2 (BMP-2) is more effective in inducing osteogenic commitment than prolonged exposure to high soluble concentrations. Based on this rationale, PLGA (Resomer® RG 502 H, 7–17 kDa) was selected as the carrier material due to its established biocompatibility, predictable degradation behaviour, and capacity to provide rapid release profiles, particularly when formulated as NCs with a diameter of approximately 150 nm and narrow size distribution. Microfluidic-assisted nanoprecipitation was employed to obtain properly uniform particles (mean size 140 ± 40 nm), ensuring reproducibility and controlled loading efficiency. The nanometric size confers a high surface-to-volume ratio, favoring an early and localized release phase of the encapsulated BMP-2. This short-term delivery is designed to coincide with the critical early

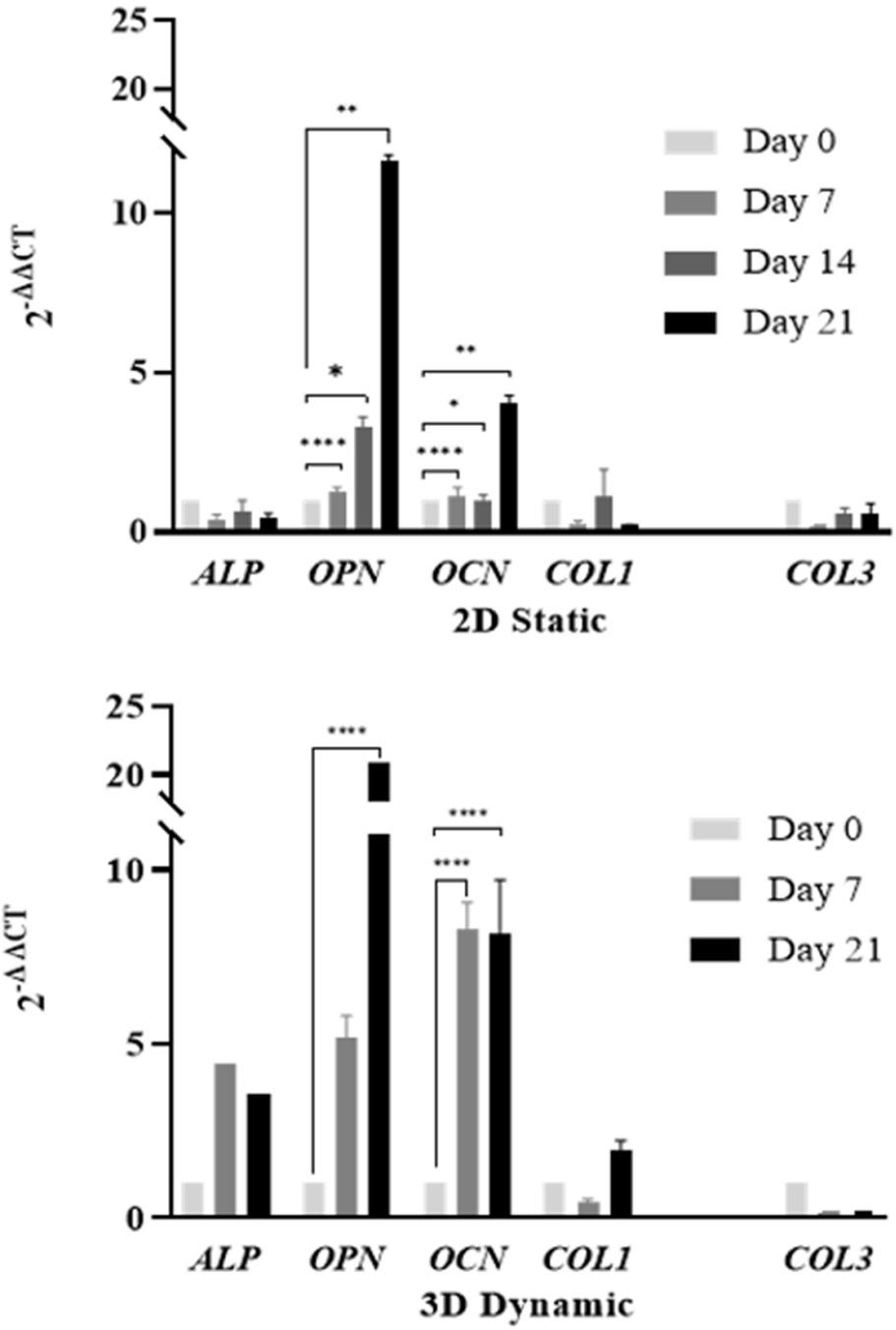

Figure 6. Quantitative real-time PCR (qRT-PCR) analysis of osteogenic gene expression in hTSPCs cultured under different conditions over 21 d. hTSPCs were either maintained in conventional 2D monolayer static culture with soluble BMP-2 supplementation (20 ng ml^{-1}) or cultured within 3D bioprinted GelMA scaffolds under dynamic perfusion, where BMP-2 was delivered via PLGA nanocarriers (NCs). The mRNA expression levels of key osteogenic markers: alkaline phosphatase (ALP), osteopontin (OPN), osteocalcin (OCN), collagen type I alpha 1 (COL1A1), and collagen type III alpha 1 (COL3A1) were quantified. Gene expression was normalized to GAPDH and expressed as fold change relative to day 0 (collected cells immediately before seeding or bioprinting). Overall, hTSPCs cultured in the 3D perfused environment exhibited significantly earlier and higher osteogenic gene expression compared to 2D cultures. Data represent mean ± SD from three independent biological replicates ($n = 3$). Statistical significance is indicated as $^{*}p < 0.05$; $^{**}p < 0.005$; $^{****}p < 0.0005$.

differentiation window (days 1–5 of culture), providing a timely inductive stimulus. Such an approach reduces the risk of cytotoxicity or off-target effects associated with supra-physiological soluble doses, while still delivering sufficient signaling to prime hTSPCs toward osteogenic commitment.

Consistent with this design, the observed rapid release of BMP-2 during the first six days aligns well with the temporal requirements of early osteogenic stimulation in tendon stem cell differentiation, underscoring the potential of this nano-reservoir system. Rather than pursuing sustained delivery,

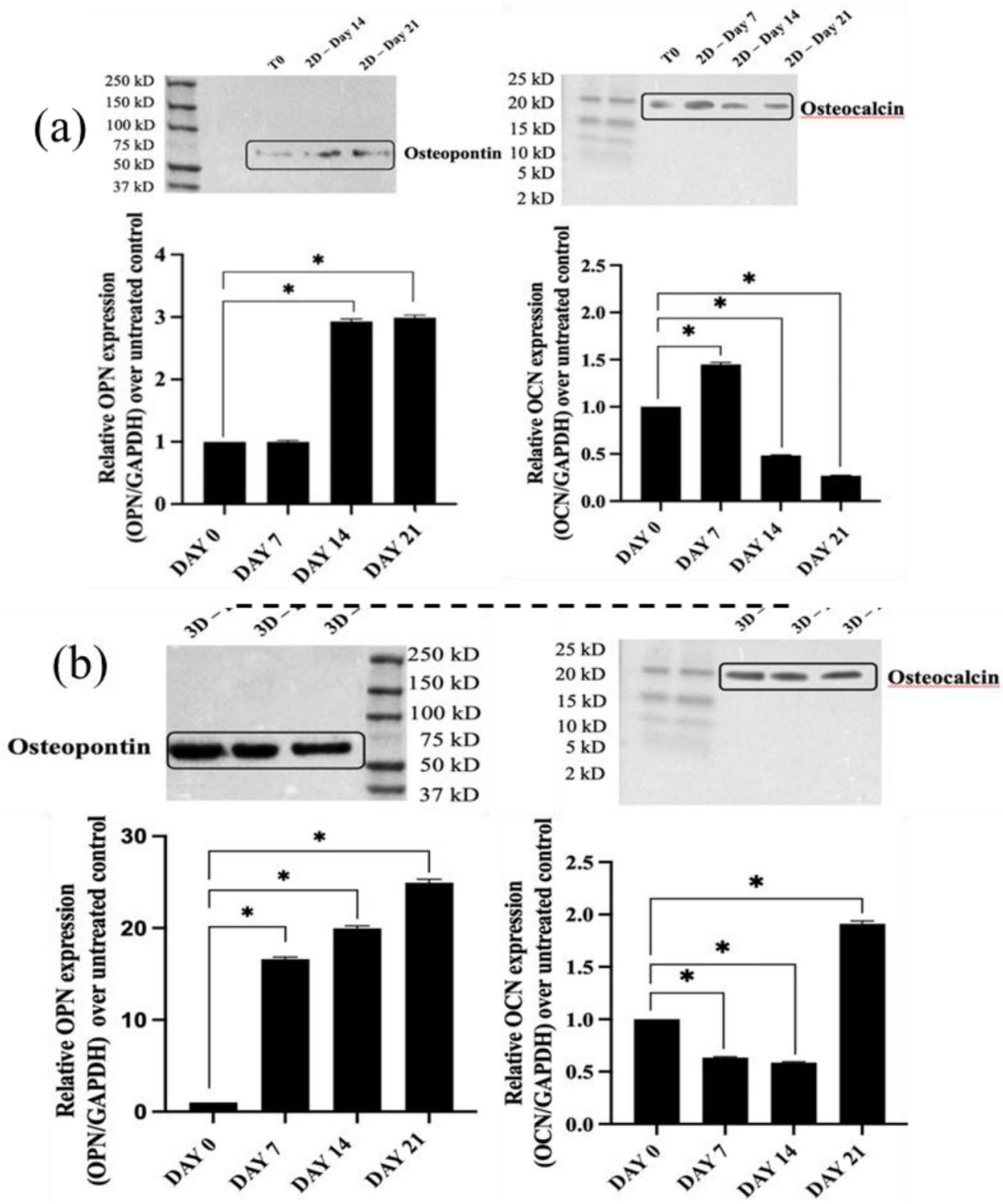

Figure 7. Western blot analysis and quantitative densitometry of osteogenic protein expression in hTSPCs cultured under different conditions over 21 d. hTSPCs were either maintained in conventional 2D monolayer static culture supplemented with soluble BMP-2 (20 ng ml^{-1}) (a) or cultured within 3D bioprinted GelMA scaffolds under dynamic perfusion, where BMP-2 was delivered via PLGA-NCs (b). Protein expression levels of osteopontin (OPN) and osteocalcin (OCN) were quantified at days 7, 14, and 21. Densitometric analysis was normalized to GAPDH and expressed as fold change relative to day 0 (cells collected immediately prior to seeding or bioprinting). hTSPCs cultured in the 3D perfused NC-based system exhibited earlier onset and significantly higher deposition of osteogenic proteins compared with 2D static cultures (see different scale bar for osteopontin between 2D vs 3D culture). Data are presented as mean ± SD from three independent biological replicates ($n = 3$). Statistical significance is indicated as $^{*}p < 0.05$; $^{**}p < 0.005$; $^{****}p < 0.0005$.

the strategy focuses on triggering osteogenic pathways through a brief, localized pulse of hBMP-2 released from PLGA NCs embedded within the printed hydrogel matrix. This configuration prioritizes early pathway activation while limiting overall exposure. These findings are in agreement with previous studies in which PLGA NCs loaded with various growth factors were incorporated into cast hydrogels to guide stem cell differentiation toward specific musculoskeletal lineages [21, 22].

GelMA at 6% w/V was chosen specifically because of its well-characterized degradation kinetics. Indeed, as reported by Yue *et al* [7], GelMA hydrogels in the 5%–10% w/V range exhibit high structural stability in physiological buffers (PBS), with less than 30% mass loss after 21 d. In the presence of differentiated cells,

the scaffold was reported to typically degrades over a period of approximately 2–4 weeks, a degradation timeframe who closely matches the 21 day osteogenic differentiation window investigated in our study.

GelMA, like most bioinks, exhibits thixotropic behavior, meaning that its viscosity decreases under applied mechanical stress. This shear-thinning property reduces printing-induced shear forces and helps limit cell damage during the bioprinting process [44–46]. The incorporation of PLGA NCs (PLGA-NCs) into the extruded GelMA mastermix did not significantly affect the hydrogel's dynamic viscosity (figure 2(d)), and good printability was preserved. However, a slight reduction in post-printing cell viability was observed, decreasing to approximately 85%, compared to the 90% survival rate previously reported for the same cells printed under similar conditions in ColMa bioink without NCs [36]. This modest decrease in viability may be attributed to additional shear stresses experienced by the cells during extrusion in the presence of the NCs, a phenomenon that has also been reported in previous studies [47, 48].

The 3D bioprinting of MSCs using alginate-based hydrogels incorporating hBMP-2–loaded PLGA-NCs has been previously reported [31], and several reviews have highlighted the benefits of nanomaterial integration to enhance bioink functionality and growth factor delivery. However, the incorporation of BMP-2–loaded PLGA-NCs within a GelMA matrix, combined with primary hTSPCs to drive their osteogenic differentiation, has not been previously described. First, osteogenic differentiation of hTSPCs remains relatively unexplored, as bone marrow-derived MSCs are typically selected as the standard cellular model for osteogenesis [15, 49–51]. In this sense, hTSPCs constitute a clinically relevant, tissue-specific primary stem cell population with distinct mechanobiological responses and differentiation potential compared to MSCs, rendering them particularly suited for applications targeting tendon-to-bone interface regeneration. More importantly, tenogenic commitment of hTSPCs dynamic culture within 3D hydrogel with growth factor supplemented medium have been previously investigated [21, 36].

The present study builds upon this prior work by demonstrating that nanoparticle-mediated BMP-2 delivery within a bioprinted GelMA scaffold can effectively direct osteogenic commitment of hTSPCs, thereby extending their previously reported behavior into a controlled tenoinductive 3D microenvironment.

The absence of perfusion reduced progressively cell viability within 3D culture [21, 22]. For this reason, perfusion bioreactor was chosen in this study, and proposed modeling, clearly demonstrated that convective mass transport for nutrients and catabolites is critical to maintain cell viability and functionality in the 3D environment. Described mass transfer also prevented the accumulation of toxic metabolic by-products, such as lactate, ultimately favoring both cell proliferation and calcium phosphate deposition. It is also our opinion that by promoting the efficient clearance of metabolic by-products, convective flow contributes to a more favorable microenvironment for both cell proliferation and differentiation. In addition, perfusion maintained sink conditions for NC-mediated release and prevents local pH reduction caused by PLGA degradation [22], thereby ensuring a proper release profile in the nearby PLGA-NCs microenvironment.

When perfusion was applied without supplementation of specific growth factors, TPSCs did not differentiate into any specific phenotype, consistent with previous reports [36]. On the contrary, in our experimental set up, calcium deposition was clearly revealed by Alizarin Red staining within the 3D matrix and significantly influence the mechanical properties of the matrix collected after 21 d of culture. The mineralization process, resulting from the deposition of calcium salts, clearly enhanced the scaffold's stiffness and structural robustness, as demonstrated by the matrix destruction that required press milling, before mRNA extraction.

Gene expression data corroborated proper osteogenesis commitments, with all key osteogenic markers, such as *ALP, OPN, OCN*, and *COL1A1*, showing significant upregulation mainly in the 3D dynamic environment. *OCN*, a late-stage osteogenic marker, exhibited a 4.06-fold increase in static conditions at day 21. Under dynamic conditions, it showed an 8-fold increase (p-value < 0.05) on both days 7 and 21; this earlier and sustained expression in dynamic conditions aligns with previous studies demonstrating that 3D culture promotes late-stage osteogenic marker expression, supporting bone-like tissue formation [15]. Type I Collagen (*COL1A1*) expression, interestingly, was nearly absent in static conditions but increased 4-fold in dynamic conditions at day 21. Conversely, type III Collagen (*COL3A1*), was downregulated throughout the 3D dynamic culture, indicating proper matrix maturation, as this collagen type is typically associated with early, less mineralized ECM; whereas, its persistence in static culture suggests a different trend, potentially reflecting delayed matrix remodeling and less favorable conditions for osteogenesis [11–14]. The overall gene expression data further confirmed the multipotency of human hTSPCs, demonstrating their successful commitment to the osteogenic lineage.

Protein-level analysis by Western blot validated the gene expression trends. Sustained OCN and strongly upregulated OPN expression in 3D scaffolds reinforce the idea that such environments provide crucial spatial and temporal cues. Notably, OCN was undetectable after day 7 in static cultures but increased progressively in 3D conditions,

confirming delayed but continuous osteogenic commitment under dynamic perfusion.

5. Conclusions and perspectives

By bioprinting PLGA NCs loaded with BMP-2 directly into GelMA-based scaffolds, we engineered a 3D microenvironment that synergistically integrates the osteoinductive potential of BMP-2, the biocompatibility of GelMA, and the benefits of a dynamic 21 d perfusion culture system. We provide functional evidence linking controlled BMP-2 release from PLGA-NCs to osteogenic commitment of hTSPCs, demonstrating successful bioprinting with excellent cell viability and lineage-specific differentiation. qRT-PCR and Western blot analyses showed strong upregulation of osteogenic markers, including osteopontin (OPN) and osteocalcin (OCN), establishing a direct functional relationship between nanoparticle-mediated growth factor delivery and stem cell behavior, a result not previously demonstrated using conventional MSCs or other models. Confocal imaging and quantitative analysis confirmed homogeneous NC incorporation within the hydrogel, addressing concerns about nanoparticle localization and demonstrating reproducible, functional scaffolds suitable for translational applications.

The NC-integrated 3D scaffolds further benefit from dynamic perfusion culture, which enhances mass transfer, ensures proper BMP-2 release kinetics, and facilitates nutrient delivery and waste clearance. Beyond osteogenesis, this GelMA-PLGA system provides a versatile platform for co-delivery of osteogenic and tenogenic cues, enabling future engineering of complex tissue interfaces such as the tendon-bone enthesis. Demonstrated in primary human cells, this approach represents a conceptual advance over prior work focused solely on bone differentiation and offers a promising strategy for both *in vitro* modeling and the development of bioengineered grafts for tendon-bone interface regeneration.

Acknowledgment

This manuscript acknowledges COST Action TENET CA22170 (European Cooperation in Science and Technology) for supporting PhD short mobility.

Data availability statement

All data that support the findings of this study are included within the article (and any supplementary files).

Supplementary data 1 available at https://doi.org/10.1088/1748-605X/ae574c/data1.

Supplementary Figure 1 available at https://doi.org/10.1088/1748-605X/ae574c/data2.

Ethics approval statement

The study was conducted in accordance with the Declaration of Helsinki and approved by the Institutional Review Board of San Giovanni di Dio e Ruggi D'Aragona Hospital (Salerno, Italy) (Review Board prot./SCCE n. 151 achieved on 29 October 2020).

Informed consent statement

Informed consent was obtained from all subjects involved in the study. Written informed consent has been obtained from the patient(s) to publish this paper.

Conflicting of interests

The author(s) declared no potential conflicts of interest with respect to the research, authorship, and/or publication of this article.

Funding

This project was funded by the University of Salerno FARB2023 Prof. Giovanna Della Porta. This project has also received partial funding from the European Union's Horizon 2020 Research and Innovation Program under the Marie Skłodowska-Curie Grant Agreement, No. 955685 (www.p4fit.eu).

Author contributions

Erwin Pavel Lamparelli 0000-0001-9700-5809
Data curation (equal), Investigation (equal), Methodology (equal), Validation (equal)

Adamo Lancellotti 0009-0008-8378-116X
Data curation (equal), Formal analysis (equal), Writing – original draft (equal)

Luigi Manzo 0009-0005-5727-7478
Data curation (equal), Formal analysis (equal)

Giacomo Cortella 0000-0002-4272-5953
Methodology (equal)

Antonio D'Ambrosio 0009-0006-6921-6776
Formal analysis (equal), Writing – review & editing (equal)

Daniela De Cata 0009-0002-3726-1581
Formal analysis (equal), Writing – review & editing (equal)

Vincenzo Piemonte 0000-0002-2421-3938
Methodology (equal), Validation (equal), Writing – review & editing (equal)

Joseph Lovecchio 0000-0002-4721-1388
Investigation (equal), Methodology (equal), Validation (equal), Writing – review & editing (equal)

Nicola Maffulli 0000-0002-5327-3702
Data curation (equal), Supervision (equal)

Emanuele Giordano 0000-0002-8054-2875
Conceptualization (equal), Supervision (equal), Validation (equal)

Giovanna Della Porta 0000-0002-1426-0159
Conceptualization (equal), Data curation (equal), Funding acquisition (equal), Project administration (equal), Resources (equal), Supervision (equal), Validation (equal), Writing – review & editing (equal)

References

[1] Nasser M I *et al* 2023 3D bioprinting in conjunction with bone marrow mesenchymal stem cells for the treatment of bone defects *Handbook of Stem Cell Applications* ed K H Haider (Springer) pp 1–28
[2] Wu Y, Ji Y and Lyu Z 2024 3D printing technology and its combination with nanotechnology in bone tissue engineering *Biomed. Eng. Lett.* **14** 451–64
[3] Łuczak J W, Palusińska M, Matak D, Pietrzak D, Nakielski P, Lewicki S, Grodzik M and Szymański Ł 2024 The future of bone repair: emerging technologies and biomaterials in bone regeneration *Int. J. Mol. Sci.* **25** 12766
[4] Liang L, Wang S, Zhang X, Yan T, Pan X, Gao Y, Zhang X, Wang Q and Qu L 2024 Multi-site enhancement of osteogenesis: peptide-functionalized GelMA hydrogels with three-dimensional cultures of human dental pulp stem cells *Regen. Biomater.* **11** rbae090
[5] Jamshidifar E, Esfandyari-Manesh M, Motasadizadeh H, Naderizadeh S, Yourdkhani A, Samadi N and Dinarvand R 2022 Improvement of *in vitro* osteogenesis and anti-infection properties by GelMA scaffold containing levofloxacin nanoparticles and strontium microspheres for osteomyelitis *J. Mater. Sci.* **57** 13603–19
[6] Fang X, Xie J, Zhong L, Li J, Rong D, Li X and Ouyang J 2016 Biomimetic gelatin methacrylamide hydrogel scaffolds for bone tissue engineering *J. Mater. Chem. B* **4** 1070–80
[7] Yue K, Trujillo-de Santiago G, Alvarez M M, Tamayol A, Annabi N and Khademhosseini A 2015 Synthesis, properties, and biomedical applications of gelatin methacryloyl (GelMA) hydrogels *Biomaterials* **73** 254–71
[8] Van Den Bulcke A I, Bogdanov B, De Rooze N, Schacht E H, Cornelissen M and Berghmans H 2000 Structural and rheological properties of methacrylamide modified gelatin hydrogels *Biomacromolecules* **1** 31–38
[9] Levato R, Jungst T, Scheuring R G, Blunk T, Groll J and Malda J 2020 From shape to function: the next step in bioprinting *Adv. Mater.* **32** 1906423
[10] Billiet T, Vandenhaute M, Schelfhout J, Van Vlierberghe S and Dubruel P 2012 A review of trends and limitations in hydrogel-rapid prototyping for tissue engineering *Biomaterials* **33** 6020–41
[11] Ribeiro F O, Gómez-Benito M J, Folgado J, Fernandes P R, García-Aznar J M and Yamamoto M 2015 In silico mechano-chemical model of bone healing for the regeneration of critical defects: the effect of BMP-2 *PLoS One* **10** e0127722
[12] Qi J, Wu H and Liu G 2024 Novel strategies for spatiotemporal and controlled BMP-2 delivery in bone tissue engineering *Cell Transplant.* **33** 09636897241276733
[13] Sun J, Li J, Li C and Yu Y 2015 Role of bone morphogenetic protein-2 in osteogenic differentiation of mesenchymal stem cells *Mol. Med. Rep.* **12** 4230–7
[14] Del Castillo-Santaella T, Ortega-Oller I, Padial-Molina M, O'Valle F, Galindo-Moreno P, Jódar-Reyes A B and Peula-García J M 2019 Formulation, colloidal characterization, and *in vitro* biological effect of BMP-2 loaded PLGA nanoparticles for bone regeneration *Pharmaceutics* **11** 388
[15] Trucillo E, Bisceglia B, Valdrè G, Giordano E, Reverchon E, Maffulli N and Della Porta G 2019 Growth factor sustained delivery from poly-lactic-co-glycolic acid microcarriers and its mass transfer modeling by finite element in a dynamic and static three-dimensional environment bioengineered with stem cells *Biotechnol. Bioeng.* **116** 1777–94
[16] Palazzo I, Lamparelli E P, Ciardulli M C, Scala P, Reverchon E, Forsyth N, Maffulli N, Santoro A and Della Porta G 2021 Supercritical emulsion extraction fabricated PLA/PLGA micro/nano carriers for growth factor delivery: release profiles and cytotoxicity *Int. J. Pharm.* **592** 120108
[17] Lamparelli E P, Marino M, Scognamiglio M R, D'Auria R, Santoro A and Della Porta G 2024 PLA/PLGA nanocarriers fabricated by microfluidics-assisted nanoprecipitation and loaded with Rhodamine or gold can be efficiently used to track their cellular uptake and distribution *Int. J. Pharm.* **667** 124934
[18] Tabeling P 2023 *Introduction to Microfluidics* (Oxford University Press)
[19] Whitesides G M 2006 The origins and the future of microfluidics *Nature* **442** 368–73
[20] Lamparelli E P, Ciardulli M C, Scala P, Scognamiglio M, Charlier B, Di Pietro P, Izzo V, Vecchione C, Maffulli N and Della Porta G 2022 Lipid nano-vesicles for thyroid hormone encapsulation: a comparison between different fabrication technologies, drug loading, and an *in vitro* delivery to human tendon stem/progenitor cells in 2D and 3D culture *Int. J. Pharm.* **624** 122007
[21] Ciardulli M C *et al* 2021 3D biomimetic scaffold for growth factor controlled delivery: an *in-vitro* study of tenogenic events on Wharton's jelly mesenchymal stem cells *Pharmaceutics* **13** 1448
[22] Lamparelli E P, Lovecchio J, Ciardulli M C, Giudice V, Dale T P, Selleri C, Forsyth N, Giordano E, Maffulli N and Della Porta G 2021 Chondrogenic commitment of human bone marrow mesenchymal stem cells in a perfused collagen hydrogel functionalized with hTGF-β1-releasing PLGA microcarrier *Pharmaceutics* **13** 399
[23] Ciardulli M C, Lovecchio J, Parolini O, Giordano E, Maffulli N and Della Porta G 2024 Fibrin scaffolds perfused with transforming growth factor-β1 as an *in vitro* model to study healthy and tendinopathic human tendon stem/progenitor cells *Int. J. Mol. Sci.* **25** 9563
[24] Ciardulli M C, Scala P, Giudice V, Santoro A, Selleri C, Oliva F, Maffulli N and Porta G D 2022 Stem cells from healthy and tendinopathic human tendons: morphology, collagen and cytokines expression and their response to T3 thyroid hormone *Cells* **11** 2545
[25] Bi Y *et al* 2007 Identification of tendon stem/progenitor cells and the role of the extracellular matrix in their niche *Nat. Med.* **13** 1219–27
[26] Zhang C, Zhu J, Zhou Y, Thampatty B P and Wang J H C 2019 Tendon stem/progenitor cells and their interactions with extracellular matrix and mechanical loading *Stem Cells Int.* **2019** 1–10
[27] Freeman F E, Pitacco P, Van Dommelen L H A, Nulty J, Browe D C, Shin J-Y, Alsberg E and Kelly D J 2020 3D bioprinting spatiotemporally defined patterns of growth factors to tightly control tissue regeneration *Sci. Adv.* **6** eabb5093
[28] Xu H, Luo H, Chen J, Chen G, Yu X and Ye Z 2023 BMP-2 releasing mineral-coated microparticle-integrated hydrogel system for enhanced bone regeneration *Front. Bioeng. Biotechnol.* **11** 1217335

[29] Yoon J, Han H and Jang J 2023 Nanomaterials-incorporated hydrogels for 3D bioprinting technology *Nano Converg.* **10** 52
[30] Longoni A, Li J, Lindberg G J, Rnjak-Kovacina J, Wise L M, Hooper G J, Woodfield T F, Kieser D and Lim K 2021 Strategies for inclusion of growth factors into 3D printed bone grafts *Essays Biochem.* **65** 569–85
[31] Choe G, Lee M, Oh S, Seok J M, Kim J, Im S, Park S A and Lee J Y 2022 Three-dimensional bioprinting of mesenchymal stem cells using an osteoinductive bioink containing alginate and BMP-2-loaded PLGA nanoparticles for bone tissue engineering *Biomater. Adv.* **136** 212789
[32] Chung Y-I, Ahn K-M, Jeon S-H, Lee S-Y, Lee J-H and Tae G 2007 Enhanced bone regeneration with BMP-2 loaded functional nanoparticle–hydrogel complex *J. Control. Release* **121** 91–99
[33] Cricchio V, Best M, Reverchon E, Maffulli N, Phillips G, Santin M and Della Porta G 2017 Novel superparamagnetic microdevices based on magnetized PLGA/PLA microparticles obtained by supercritical fluid emulsion and coating by carboxybetaine-functionalized chitosan allowing the tuneable release of therapeutics *J. Pharm. Sci.* **106** 2097–105
[34] Rui Y F, Lui P P Y, Lee Y W and Chan K M 2012 Higher BMP receptor expression and BMP-2-induced osteogenic differentiation in tendon-derived stem cells compared with bone-marrow-derived mesenchymal stem cells *Int. Orthop.* **36** 1099–107
[35] Dai G, Li Y, Liu J, Zhang C, Chen M, Lu P and Rui Y 2020 Higher BMP expression in tendon stem/progenitor cells contributes to the increased heterotopic ossification in achilles tendon with aging *Front. Cell Dev. Biol.* **8** 570605
[36] Cortella G, Lamparelli E P, Ciardulli M C, Lovecchio J, Giordano E, Maffulli N and Della Porta G 2025 ColMA - based bioprinted 3D scaffold allowed to study tenogenic events in human tendon stem cells *Bioeng. Transl. Med.* **10** e10723
[37] Cortella G, Lamparelli E P, Lovecchio J, Giordano E, Maffulli N and Della Porta G 2025 A 3D ColMA-based tenogenic microenvironment unveils the behavior of tendon stem/progenitor cells (TSPCs) from tendinopathic surgical explants *Bioengineering* **12** 1337
[38] Clerici M, Citro V, Byrne A L, Dale T P, Boccaccini A R, Della Porta G, Maffulli N and Forsyth N R 2023 Endotenon-derived type II tendon stem cells have enhanced proliferative and tenogenic potential *Int. J. Mol. Sci.* **24** 15107
[39] Citro V, Clerici M, Porta G D, Maffulli N, Boccaccini A R, Dale T P and Forsyth N R 2025 Tenogenic cues are biochemically and environmentally distinct for tendon stem cells and mesenchymal/stromal stem cells *Stem Cells Int.* **2025** 9047956
[40] Pasini A, Lovecchio J, Ferretti G and Giordano E 2019 Medium perfusion flow improves osteogenic commitment of human stromal cells *Stem Cells Int.* **2019** 1–10
[41] Lamparelli E P, Ciaglia E, Ciardulli M C, Lopardo V, Montella F, Puca A A and Della Porta G 2025 Optimizing mRNA delivery: a microfluidic exploration of DOTMA vs. DOTAP lipid nanoparticles for GFP expression on human PBMCs and THP-1 cell line *Int. J. Pharm.* **672** 125324
[42] Treybal R E 2004 *Mass-transfer Operations* 3rd edn reissued (McGraw-Hill chemical engineering series) p 784
[43] Dvorak N 2023 Performance of a flexible bioreactor for tendon tissue engineering *Doctoral Dissertation* University of Oxford
[44] El-Sherbiny I M and Yacoub M H 2013 Hydrogel scaffolds for tissue engineering: progress and challenges *Glob. Cardiol. Sci. Pract.* **2013** 38
[45] Cooke M E and Rosenzweig D H 2021 The rheology of direct and suspended extrusion bioprinting *APL Bioeng.* **5** 011502
[46] Ardaneh F, Immonen E, Chaudhari A, Pelkonen J and Knuutinen S 2024 Analysis of viscosity behaviour of shear-thinning hydrogels in 3d-printing nozzles *ECMS 2024 Proc.* (*Accessed 25 September 2025*) ed D Grzonka, N Rylko, G Suchacka and V Mityushev (ECMS) pp 359–65 (available at: www.scs-europe.net/dlib/2024/2024-0359.html)
[47] Kapur S, Baylink D J and William Lau K-H 2003 Fluid flow shear stress stimulates human osteoblast proliferation and differentiation through multiple interacting and competing signal transduction pathways *Bone* **32** 241–51
[48] Boularaoui S, Al Hussein G, Khan K A, Christoforou N and Stefanini C 2020 An overview of extrusion-based bioprinting with a focus on induced shear stress and its effect on cell viability *Bioprinting* **20** e00093
[49] Du L, Qin C, Zhang H, Han F, Xue J, Wang Y, Wu J, Xiao Y, Huan Z and Wu C 2023 Multicellular bioprinting of biomimetic inks for tendon-to-bone regeneration *Adv. Sci.* **10** 2301309
[50] Rosset J, Olaniyanu E, Stein K, Almeida N D and França R 2024 Exploring the frontier of 3D bioprinting for tendon regeneration: a review *Eng* **5** 1838–49
[51] Wang Y, Chen C, Zhang C, Cheng J, An B, Zhang N, Liu J and Wang Z 2025 3D bioprinting for tendon-bone interface regeneration *Int. J. Bioprint.* **11** 8411